INORGANIC CHEMISTRY FRONTIERS

RESEARCH ARTICLE

View Article Online
View Journal | View Issue

Check for updates

Cite this: *Inorg. Chem. Front.*, 2026, **13**, 3154

Bimetallic Fe–Ni exsolution from A site deficient $SrTiO_3$: insight into the reciprocal role of metal active centers

Pietro Mariani,[a] Jacopo Orsilli,[a,b] Henk Stoffel,[c] Simone Mascotto,[c] Damiano Monticelli,[d] Enrico Berretti,[e] Alessandro Lavacchi,[e] Luca Bignardi,[f,g] Cinzia Cepek,[g] Maria A. Goula,[h] Nikolaos D. Charisiou,[h] Angeliki I. Latsiou,[h] Silvia Mostoni,[a] Barbara Di Credico,[a] Roberto Scotti[a] and Massimiliano D'Arienzo *[a]

In this work, we examine the redox behavior and exsolution kinetics of Ni and Fe in A-site-deficient $Sr_{0.95}Ti_{1-x+y}Fe_xNi_yO_{3\pm\delta}$, combining TPR, XAS, electron microscopy and EPR to elucidate dopant-specific contributions to defect chemistry and metal nucleation. In particular, TPR data indicated that Fe predominantly governs the formation and reducibility of oxygen-vacancy-associated defects, generating reduced Fe species at comparatively low temperature, whereas Ni dictates the overall reduction extent. In fact, as assessed by XAS, Ni-only samples exhibit relatively low conversion to Ni(0), while co-doping with Fe boosts Ni exsolution. Moreover, it turned out that even a tiny Ni amount promotes iron reduction, as unveiled by EXAFS. Along this line, STEM analyses confirmed the surface segregation of well-anchored Fe–Ni co-exsolved nanoparticles for co-doped perovskites, while scarce exsolution was observed for Fe-doped samples. EPR completed the picture corroborating that Fe species, incorporated in the perovskite as highly stable Fe(III) substitutional defects, are less reducible and less mobile than Ni ones, which instead appear mostly as intercalated sites. Such Fe defects become mobile and undergo surface segregation only when Ni is incorporated in the lattice. These structure–property relationships directly translate into enhanced performance in the RWGS reaction of co-doped perovskites, where Fe drives vacancy-mediated redox processes while Ni promotes H_2 dissociation. Overall, the results indicate that the methodological approach developed here can be extended to other exsolvable dopants (*e.g.*, Co), offering a pathway toward the rational design of exsolved catalysts with tunable structures and compositions for advanced energy-conversion applications.

Received 7th December 2025,
Accepted 1st February 2026

DOI: 10.1039/d5qi02469b

rsc.li/frontiers-inorganic

Open Access Article. Published on 03 febbraio 2026. Downloaded on 31/05/2026 00:22:16.
This article is licensed under a Creative Commons Attribution-NonCommercial 3.0 Unported Licence.

Introduction

Over the past few years, the redox exsolution process from doped perovskite has gained great interest from the scientific community due to the possibility of delivering tailorable, highly stable, selective, and regenerative catalysts.[1] Exsolution occurs when a doped perovskite oxide is reduced under high-temperature in an oxygen-deficient atmosphere. As oxygen is released from the crystal lattice, transition metal dopants get reduced to their elemental form. Through spontaneous nucleation and growth, metal nanoparticles migrate from the bulk to the oxide surface, generating "socketed" metal catalysts which offer superior stability, less susceptibility to deactivation, and regeneration possibility compared to conventional impregnated systems, exsolved nanoparticles.[2–6]

It is worth noting that certain metals, such as Fe, are unlikely to exsolve when they are the sole B-site cation in the perovskite lattice due to their high segregation energy. However, co-exsolution can be achieved by incorporating a second, more reducible metal—such as Ni or Co—with a lower segregation energy.[7–9] In mixed B-site systems, the Gibbs free energy of reduction is influenced by the metal–oxygen bond strengths of

[a]*University of Milano-Bicocca, Dept. of Materials Science, INSTM, Via R. Cozzi 55, 20125 Milano, Italy. E-mail: massimiliano.darienzo@unimib.it*
[b]*CNR – Istituto Officina dei Materiali (IOM), c/o ESRF LISA CRG, Avenue des Martyrs 71, Grenoble 38000, France*
[c]*Institut für Integrierte Naturwissenschaften, Univertsität Koblenz, Germany*
[d]*University of Insubria, Dept. of Science and High Technology, Via Valleggio 11, Como, Italy*
[e]*Institute of Chemistry of the Organometallic Compounds – National Research Council (ICCOM-CNR), Via Madonna del Piano, 10, 50019 Sesto Fiorentino (FI), Italy*
[f]*Department of Physics, University of Trieste, via Valerio 2, 34127 Trieste, Italy*
[g]*Istituto Officina dei Materiali-CNR Laboratorio TASC, Strada Statale 14, km 163.4, I-34012 Trieste, Italy*
[h]*Laboratory of Alternative Fuels and Environmental Catalysis (LAFEC), Department of Chemical Engineering, University of Western Macedonia, GR-50100 ZEP, Greece*

This journal is © the Partner Organisations 2026

Open Access Article. Published on 03 febbraio 2026. Downloaded on 31/05/2026 00:22:16.
This article is licensed under a Creative Commons Attribution-NonCommercial 3.0 Unported Licence.

both cations. Consequently, introducing more reducible species can lower the overall energy barrier and facilitate exsolution.[6] The process typically results in the formation of alloy nanoparticles at the surface, as supported by several modelling and experimental studies.[10,11] Exsolution is driven by oxygen vacancies generated during the reduction process, which tend to migrate from the bulk toward the surface. This migration promotes the segregation of reducible metal species alongside oxygen vacancies, as less energy is required.[12]

In particular, as concerns Fe–Ni bimetallic systems, Irvine *et al.*[13] demonstrated that in $(La_{0.75}Sr_{0.25})(Cr_{0.5}Fe_{0.5-x}Ni_x)O_3$ stoichiometric perovskite, the exsolution of Fe–Ni alloy nanoparticles from the B-site takes place, leading to the formation of a Ruddlesden Popper (RP) phase similar to $(La,Sr)_{m+1}(Cr,Fe)_mO_{3m+1}$. The exsolution process initiates in proximity to the surface. Upon reduction of the perovskite, cation diffusion occurs from the subsurface layers toward the surface. Consequently, an RP-type phase forms as a shell encapsulating the perovskite particles. In their study, it was also noticed that the exsolved alloy nanoparticles exhibited a higher Ni content compared to Fe. This observation is attributed to the lower Gibbs free energy associated with the reduction of NiO to metallic Ni, relative to that of Fe_2O_3 to metallic Fe, as reported by Neagu *et al.*[14] Consequently, the reduction of Ni^{2+} to Ni(0) is thermodynamically more favorable than the reduction of Fe^{3+} to Fe(0).

Some of the authors[15] also recently investigated Fe–Ni bimetallic exsolution in highly doped La-doped $SrTiO_3$, highlighting that the Fe/Ni exsolution ratio was directly connected to the oxygen vacancy concentration associated with Fe. For lower vacancy concentration more Ni than Fe was exsolved, but when the vacancy concentration increased the amount of exsolved Fe overtook the Ni one.

In general, Ni was found to reduce more readily than Fe, with XRD and TEM analyses confirming the formation of the Ni_3Fe intermetallic phase. Despite these observations, so far the mutual reduction process of Ni and Iron is not understood, and more studies are needed for the design of bimetallic nanoparticles *via* exsolution.

In addition to the aforementioned fundamental and mechanistic investigations, the majority of studies on Fe–Ni bimetallic exsolution reported in the current literature are application-oriented. These works not only highlight the significant performance enhancements associated with the Ni–Fe interfacial synergy but also emphasize the limited reversibility of the exsolution process as a critical challenge for practical implementation.

Besides the wide application as electrocatalytic materials,[16,17] exsolved Fe–Ni alloy systems have also been employed as catalytic materials for various thermochemical reactions including methane reforming,[18] CO oxidation,[19] and, albeit to a lesser extent, also in reverse water gas shift (RWGS)[20] Regarding the former, the influence of A-site cations on catalytic performance was systematically studied in a series of $LnFe_{0.7}Ni_{0.3}O_{3-\delta}$, (Ln = La, Pr, Sm) perovskites. Among these, the $PrFe_{0.7}Ni_{0.3}O_{3-\delta}$ composition demonstrated the highest catalytic activity and stability, attributed to the optimized composition of exsolved Fe–Ni nanoparticles characterized by a higher Fe content.[18] Furthermore, increasing the Ni doping level was found to enhance the oxygen non-stoichiometry of the perovskite structure. This was ascribed to the reduction of Fe^{3+}/Fe^{4+} and Ni^{2+} to lower oxidation states, which promoted Fe–Ni nanoparticle exsolution and led to significantly improved catalytic activity for CH_4 conversion.[13] In the case of CO oxidation, exsolved Fe–Ni nanoparticles derived from $La_{0.5}Sr_{0.4}Fe_{0.1}Ni_{0.1}Ti_{0.6}O_3$ exhibited not only high catalytic activity, but also excellent long-term stability over 170 hours and notable sulfur tolerance.[19]

Finally, in the case of the RWGS reaction, Orsini F. *et al.*[20] have recently investigated the structural evolution and redox behavior of the double perovskite $Sr_2FeMo_{0.6}Ni_{0.4}O_{6-\delta}$ under H_2 and CO_2 redox cycling, with a particular focus on its performance in the Reverse Water–Gas Shift Chemical Looping (RWGS-CL) process. The study revealed that both the reduction and oxidation steps were significantly enhanced, a phenomenon attributed to the exsolution of Ni–Fe alloy nanoparticles and the concurrent formation of the RP phase $Sr_3FeMoO_{7-\delta}$. This was ascribed to the synergistic interaction between the exsolved Ni–Fe alloy nanoparticles, which facilitate the adsorption and activation of H_2 and CO_2, and the RP phase, which promotes rapid oxygen exchange during the redox cycle.

Despite this substantial body of literature, very few studies have thoroughly investigated the individual and synergistic roles of Ni and Fe in their bimetallic exsolution from A-site-deficient perovskites, particularly in the context of their specific contributions in the RWGS reaction. A very meaningful basis for further discussion and in-depth analysis of these aspects is offered by the work of Lindenthal L. *et al.*[21] Investigating the behavior of various doped and co-doped perovskite materials for the RWGS, the authors observed that the highest catalytic activity was attained when metallic nanoparticles were exsolved *in situ* during the reaction. This enhancement was attributed to a Mars–van Krevelen-type mechanism, wherein dissociative adsorption of H_2 occurs on the surface of the exsolved metal particles. The resulting active hydrogen species then migrate *via* spillover to the perovskite lattice, promoting its reduction and increasing oxygen vacancy formation, which in turn enhances CO_2 activation. Furthermore, the study proposed that incorporating an easily reducible dopant (*e.g.*, Co or Ni) at the B-site, in combination with a less reducible primary component (*i.e.*, Fe), not only facilitates the formation of metallic nanoparticles on the surface but also promotes the preferential exsolution of the dopant. Simultaneously, the presence of the more stable, less reducible host cation preserves the integrity of the perovskite lattice under reducing conditions. This structural stability enables effective anchoring of the exsolved nanoparticles, thereby mitigating sintering and maintaining a high density of gas/metal/oxide three-phase boundaries essential for catalytic activity.

These considerations prompted us to study in more detail the individual and cooperative effect of Ni and Fe in the

Open Access Article. Published on 03 febbraio 2026. Downloaded on 31/05/2026 00:22:16.
This article is licensed under a Creative Commons Attribution-NonCommercial 3.0 Unported Licence.

process of bi-metallic exsolution from A-site-deficient $SrTiO_3$ perovskite. In detail, A-site-deficient perovskite oxides of the type $Sr_{0.95}Ti_{1-x+y}Fe_xNi_yO_{3\pm\delta}$ with x = 0, 0.01, 0.05 and y = 0, 0.001, 0.01, 0.05 were successfully synthesized by using a tailored sol–gel method, while surface decoration with small (bi) metallic nanoparticles was achieved through redox exsolution. Exploiting the low doping levels and combining several characterization techniques, in particular X-ray Absorption Spectroscopy (XAS) and Electron Paramagnetic Resonance (EPR) spectroscopy, we elucidated the complementary roles of Ni and Fe in the exsolution process. We demonstrated that their action is intrinsically linked with their coordination environments and oxidation states during exsolution, which, in turn, influence the selectivity and CO_2 conversion efficiency in the RWGS reaction.

Materials and methods

Materials

Strontium nitrate (99%, Acros Organics), titanium(IV) isopropoxide (97%, Alfa Aesar), Iron(III) nitrate (98%, Alfa Aesar), Ni(II) nitrate (98%, Alfa Aesar), anhydrous citric acid (99.6%, Acros Organics), glycerol (99%, Alfa Aesar) were used as received without further purification.

Synthesis of perovskite materials

Perovskites were prepared according to a previously reported synthetic route.[22] This method involves a low-temperature pretreatment (at 400°) and lower calcination temperature and time (at 900 °C for 2 h) compared to those typically used,[23,24] ensuring the formation of a relatively pure single-phase perovskite. In particular, four different samples with general formula $Sr_{0.95}Ti_{1-x+y}Fe_xNi_yO_{3\pm\delta}$ with x = 0, 0.01, 0.05 and y = 0, 0.001, 0.01, 0.05 have been prepared. The samples were labelled as xFeyNi-STO, where x and y refer to the nominal mol mol^{-1} percentage of the Fe and Ni-dopant in the B-site.

Exsolution procedure

Exsolution/reduction treatments were carried out using a U-shaped quartz tube filled with 70 mg of each sample. 5% H_2/Ar was chosen as the reducing gas, and the flow rate was set at 100 mL min^{-1}. A ramping rate of 10 °C min^{-1} was employed to reach the final temperatures of 400 °C, 600 °C, or 900 °C with a dwell time of 1 h.

Materials characterization

Powder X-ray diffraction (PXRD) patterns were recorded using a Rigaku Miniflex 600. The acquisition was performed using a Cu source (40 kV, 15 mA), scanning in the 20–80° 2θ range, with a step size of 0.01 degrees and an angular velocity of 3.0 degrees per minute. Instrumental PDXL-2 software was used for the sake of comparison with reference diffraction patterns from the ICDD database. The mean crystallite sizes were calculated from the full width at half-maximum (FWHM) of the most intense reflection using the Scherrer equation. The concentrations of metal ions (Sr, Ti, Fe, Ni) were determined by Inductively Plasma Mass Spectrometry (ICPMS, model iCAP-Q from Thermo Scientific) after microwave assisted digestion (ETHOS One microwave digestor from Milestone) in concentrated hydrochloric acid.

Temperature-programmed reduction (TPR) measurements were carried out using a BELCAT II catalytic analyzer (Microtrac Retsch GmbH). For each measurement, a sample mass of at least 40 mg was used. Prior to the experiment, the thermal conductivity detector (TCD) was stabilized at room temperature for a minimum of 90 min. The TPR measurements were performed with a gas flow of 5% H_2 in N_2 at a flow of 20 sccm, applying a heating ramp of 10 °C min^{-1} up to 900 °C. The target temperature was maintained for 30 min. A baseline correction was applied to the TCD signal, and the resulting curves were normalized for data visualization. Hydrogen consumption was quantified using the ChemMaster II software (Microtrac Retsch GmbH).

The surface chemical composition of the sample powders was investigated by X-ray photoelectron spectroscopy (XPS). The measurements were performed on the samples in powder form, fixed on the sample holder using UHV-compatible carbon tape. The XPS spectra were acquired under ultrahigh vacuum (base pressure: $\sim 5 \times 10^{-10}$ mbar) at RT in a normal emission geometry using a conventional Mg X-ray source ($h\nu$ = 1253.6 eV) and a hemispherical electron energy analyzer (120 mm by PSP: total energy resolution ~0.8 eV). Due to charging effects, all binding energies (BE) were calibrated by fixing the BE of the Ti 2p3/2 core level relative to STO at 458.3 eV.49 Survey scans were acquired in the 0–1000 binding energy eV energy range, and detailed scans were recorded in the BE regions corresponding to C 1s, Sr 3d, Ti 2p, Ni 2p, and Fe 2p core levels. The XPS spectra were analysed by fitting the experimental data using integral background and Voigt components, corresponding to different oxidation states and chemical environments. Details of the fitting procedure and parameters are provided in the SI. The atomic ratio was calculated from the peak area and the sensitivity factor of our instrument.

A Thermo Fisher Talos F200X G2 was used for high-resolution scanning transmission electron microscopy (STEM) imaging with an acceleration voltage of 200 kV and a resolution of 4096 × 4096 pixels without any objective apertures. Super X spectrometers equipped with silicon drift detectors of 30 mm^2 were used to collect energy dispersive X-ray analysis (EDX) maps with a collection angle of 0.7 s rad.

The measurements at the Fe and Ni K-edges (7112 and 8333 eV, respectively) were carried out at the Italian CRG Beamline Lisa (BM08) at the European Synchrotron Radiation Facility (ESRF, Grenoble, France).[25] The Fluorescence yield was collected through a 4-element Peltier-cooled SDD detector.[26] To provide an accurate energy calibration, reference metal foils of Fe and Ni, placed in a second experimental chamber, located downstream from the first one, were measured concurrently. The beam flux before and after the sample, and before and after the reference metal foil, was measured using N_2-filled ionization chambers.

 This journal is © the Partner Organisations 2026

Open Access Article. Published on 03 febbraio 2026. Downloaded on 31/05/2026 00:22:16.
This article is licensed under a Creative Commons Attribution-NonCommercial 3.0 Unported Licence.

The energy of the X-ray beam was selected by a fixed exit monochromator with a pair of Si (111) crystals (energy resolution $\Delta E/E \approx 1.1 \times 10^{-4}$). At the same time, Si mirrors were used for harmonics rejection ($E_{cutoff} \approx 15$ keV). Spectral acquisitions were set up to provide a significant energy resolution in the X-ray Absorption Near Edge Structure (XANES) and Extended X-ray Absorption Fine Structure (EXAFS). Accordingly, the step size in the XANES region was 0.5 eV, and the post-edge EXAFS region of the spectrum was acquired with a fixed k-step width of 0.05 $Å^{-1}$. Measurements were carried out at room temperature and in low vacuum conditions (10^{-2} mbar).

The structure and local arrangement of Fe and Ni were examined using X-ray Absorption Spectroscopy (XAS) in both fluorescence and transmission modes. Spectra were collected from 28 samples, which were pelletized with microcrystalline cellulose. The analysis of the XAS spectra was performed using Athena and Artemis software, part of the Demeter package[27] and Larch.[28] The XAS spectrum energy was first calibrated using the reference foil, then its background was subtracted, and it was normalized using the Athena software. Finally, the XANES and EXAFS were extracted. The normalized XANES were investigated through Linear Combination Fitting (LCF) using the Larch package; the as-prepared samples' spectra, and the metal foils were employed as end-members. This procedure was performed in the energy range of −20 to +90 eV (with respect to the metal edge position). The reference spectra were used as primary components, and their weights were constrained to vary between 0 and 1, while the total weights sum was left free to vary. Theoretical EXAFS paths of iron and nickel were calculated using feff6[29] starting from the models of $SrTiO_3$ reported by ref. 30 (with a Ti substituted with Fe and Ni), using Muffin Tin potentials and the Hedin–Lundqvist approximation. The edges were analyzed in the R range, using a k^2-weight. The FT window was chosen considering the EXAFS signal-to-noise ratio to include as much oscillation as possible.

EPR measurements were performed by using a Bruker EMX spectrometer operating at the X-band frequency and equipped with an Oxford cryostat working in the temperature range of 4–298 K. A tailored home-made system was utilized, where the sample in the EPR tube can be directly heated up and connected both to a high vacuum pumping system and to a controlled gas feed (H_2/Ar 95/5 wt% and O_2) to provide a reducing or oxidation atmosphere. Spectra were recorded at a power of 20 mW under *in vacuo* conditions ($p < 10^{-5}$ mbar) and at 130 K after their thermal treatment at 400 °C, 600 °C, or 900 °C under an H_2/Ar atmosphere. Results on undoped sample are reported in our previous work.[22]

Catalyst evaluation

The activity of the prepared catalysts was evaluated in the CO_2 hydrogenation reaction using a fixed-bed quartz reactor (I.D. 0.9 cm) between 400 °C and 750 °C, H_2/CO_2 = 4/1, WHSV = 25 000 mL h^{-1} g^{-1} and P = 1 atm. 0.24 g of catalyst was diluted with an equal amount of quartz sand, and the mixture was loaded into the reactor above a layer of quartz wool. A thermocouple was placed inside the catalytic bed for monitoring the temperature during the experiment, while a cold trap was installed at the reactor outlet to collect the produced water vapor. Prior to the reaction, all catalysts were *in situ* reduced under 5% H_2/Ar (50 mL min^{-1}) with a heating ramp of 10 °C min^{-1} up to T = 900 °C, with a dwell time of 2 h. Afterwards, the reactor was cooled down at 400 °C under a flow of Ar. Then, the gas mixture switched to CO_2/H_2/Ar = 1/4/5; Ar was used as an internal standard. The total flow was set to 100 ml min^{-1} and measurements were obtained at 50 °C intervals under steady-state operation (two measurements were taken at each temperature). The gases of the reactor outlet were analysed using an online gas chromatograph (Agilent, 8890 GC), equipped with TCD and FID detectors. CO and CH_4 were the only products detected during the experiments.

Results and discussion

Structural and morphological characterization of parental materials

The elemental composition of the synthesized samples was verified by ICP analysis, which confirmed their nominal stoichiometry (see Table S1, SI). Their crystalline phase structures were characterized using powder X-ray diffraction (PXRD), and the results for some representative samples are summarized in Fig. 1. All the powders display the same crystalline structure corresponding to the cubic $Pm\bar{3}m$ structure of the $SrTiO_3$ perovskite oxide,[31] with only small impurity phases present between 2θ = 20°–30°, attributable to $SrCO_3$ and TiO_2, which are commonly found impurities in these kinds of materials.[32]

To further elucidate the oxidation state and local environment of the Fe and Ni dopants, X-ray absorption spectroscopy (XAS) measurements were carried out. The spectra of the as-prepared Fe-STO, Ni-STO, and co-doped FeNi-STO samples were measured at the Fe and Ni K-edges (7112 and 8333 eV, respectively). From a general point of view, the comparison of

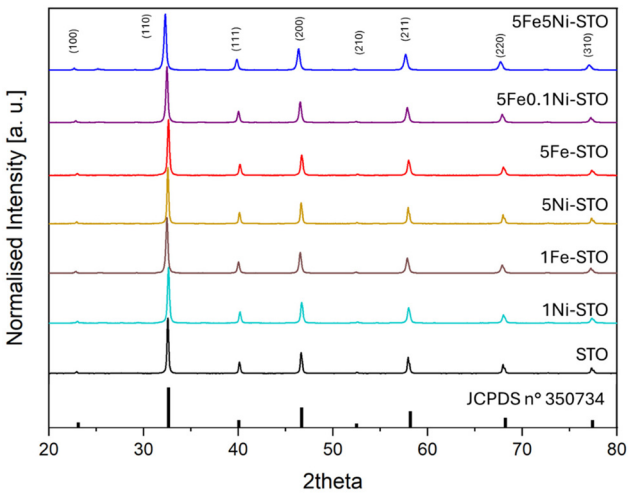

Fig. 1 PXRD diffractogram of pure STO, 5Fe-STO, 5Ni-STO and 5Fe5Ni-STO samples.

Open Access Article. Published on 03 febbraio 2026. Downloaded on 31/05/2026 00:22:16.
This article is licensed under a Creative Commons Attribution-NonCommercial 3.0 Unported Licence.

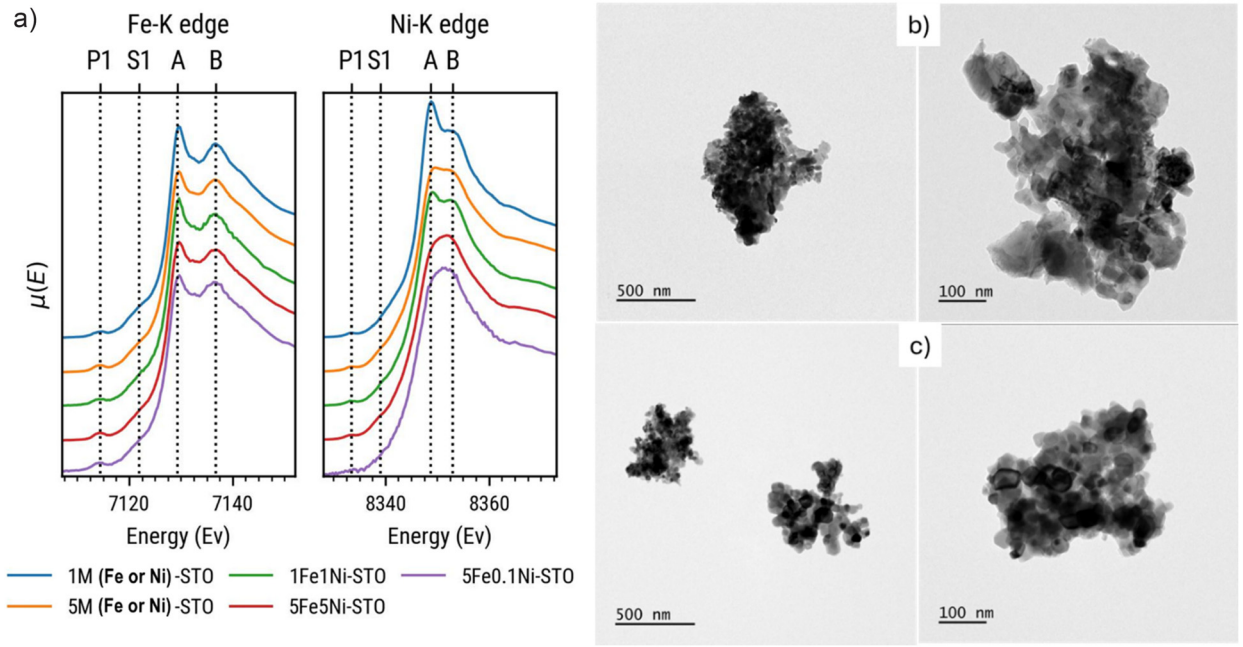

Fig. 2 (a) XAS spectra of all the as-prepared doped and co-doped perovskite samples; (b and c) representative TEM images of the 5Fe-STO and 5Fe5Ni-STO parental structures.

the XANES spectra (Fig. 2a) with literature data[33] suggests that both Fe and Ni are inside the perovskite structure, as substitutes for Ti. In detail, in the case of Fe, we observe two peaks (A and B) at 7129.3 and 7136.8 eV, indicative of the perovskite structure, a pre-peak (P1) at 7114.4 eV, characteristic of the 1s → 3d quadrupole transition of Fe(III), and a shoulder (S1) at 7122 eV due to the 1s → 4d dipole transition.[33] The structure of the spectra does not appear to change with the dopant concentration. Ni spectra show a similar shape: two peaks (A and B) at 8348.7 and 8353 eV, indicating its substitution of Ti in the perovskite structure, a pre-peak P1 at 8333.5 eV (less intense than in the Fe spectra), and a shoulder S1 at 8339 eV. However, for nickel, we observe a higher variability in the XANES region. In fact, we can clearly see that 1Ni-STO sample better represents the perovskite spectrum (peaks A and B are well-resolved), whereas for the other powders spectra present lower peaks, indicating a deviation from the structure. The same can be inferred by observing the Fourier Transform (Fig. S1 in SI), in which we observe a decrease in signal related to the first shell (Ni–O), and to a higher extent of the second and third shells (Ni–Sr and Ni–Ti/Ni bonds).

Representative TEM images of 5Fe-STO and 5Fe5Ni-STO are presented in Fig. 2b and c. The powders show large aggregates of nanoparticles, displaying size varying between ~50 to ~100 nm. Any significant variation, both in terms of morphological features and particle dimensions, was observed for the other perovskite compositions.

Exsolution monitoring

The exsolution process was first monitored with TPR to get insights into the reduction of the materials during the high-temperature treatment with hydrogen. In detail, the TPR profiles of the Ni-doped and Fe-doped compounds compared to the bare STO sample are shown (Fig. 3). Concerning the Ni-doped materials (Fig. 3a), a clear influence of the dopant concentration is observed. The undoped STO sample exhibits a broad reduction signal between 530 °C and 790 °C, which can be attributed to lattice oxygen release from the A-site-deficient perovskite structure (hydrogen uptake of 0.219 mmol g^{-1}). Upon 1% Ni doping (1Ni-STO), the overall reduction profile is preserved; however, enhanced oxygen release is observed at 600 °C and, more prominently, at 800 °C, with a total hydrogen consumption of 0.488 mmol g^{-1}. This behavior suggests that Ni species are mainly substitutional at Ti sites—consistent with observations for other dopants[22] and that reduction is activated only at elevated temperatures.

When the Ni content increases to 5% (5Ni-STO) the consumption of hydrogen increases up to 0.807 mmol g^{-1} and an additional reduction contribution emerges at approximately 400 °C. Simultaneously, the feature at ~600 °C gains intensity, while the one at 800 °C markedly decreases. These variations indicate that the Ni species occupy different sites within the structure. The lower reduction temperature and enhanced 600 °C signal imply the presence of a larger fraction of Ni species located at or near the surface, or less incorporated into the perovskite lattice. Conversely, the diminished 800 °C signal indicates a reduced amount of substitutional Ni in the bulk.

For the Fe-doped systems, the reduction profiles closely resemble that of the undoped STO (Fig. 3b). This is not unexpected, since Fe can readily substitute Ti in its lattice positions,[31,32] thereby maintaining a similar point defect

 This journal is © the Partner Organisations 2026

Open Access Article. Published on 03 febbraio 2026. Downloaded on 31/05/2026 00:22:16.
This article is licensed under a Creative Commons Attribution-NonCommercial 3.0 Unported Licence.

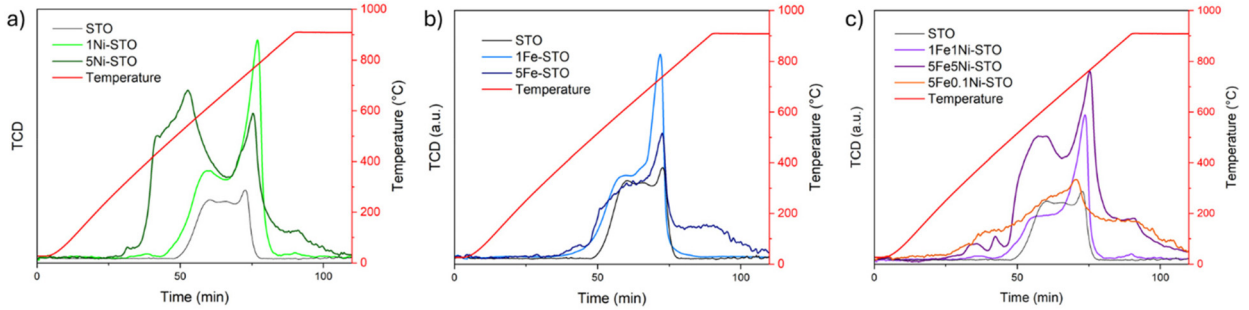

Fig. 3 TPR profiles of (a) Ni-doped and (b) Fe-doped and (c) Fe-Ni co-doped perovskites powders. The behavior of undoped STO sample is reported for comparison.

structure. Nevertheless, due to the higher number of oxygen vacancies introduced by Fe doping,[15] an overall increase in oxygen release and thus higher hydrogen consumption with respect to the pristine STO material is observed (0.306 mmol g^{-1}). The 5% Fe-doped material, similar to 5Ni-STO, displays a lower intensity of the 800 °C peak but sustains a significant H_2 consumption up to 900 °C (0.357 mmol g^{-1}), indicating a higher concentration of substitutional defect species in the lattice, and the possible reduction of Fe(II) to metallic Fe, which is not evident in the 1Fe-STO sample.

Finally, the reduction behavior of the Ni–Fe co-doped materials exhibits distinctive features (Fig. 3c). When the Fe concentration is equal to or lower than that of Ni, the reduction profile largely overlaps with that of pure STO, except for a higher overall intensity due to the increased oxygen vacancy concentration. This suggests that the defect structure remains largely unchanged. However, when the Fe content exceeds the Ni content, a markedly different reduction behavior appears. Regardless of the Ni amount, the reduction process becomes active at temperatures as low as 300 °C and continues steadily beyond the main reduction peak, with constant H_2 consumption up to 900 °C. The intensity of the main region between 500 °C and 800 °C scales with the Ni content in the samples. The weak shoulder observed at around 610 °C in 5Fe0.1Ni-STO evolves into a broad and more intense feature, reflecting higher hydrogen consumption. Moreover, this peak is further shifted toward lower temperatures. A peak at around 790 °C is present in all co-doped compounds, whose intensity increases alongside the Ni content.

From these observations, we may infer that Fe doping, and the resulting formation of oxygen-vacancy-related defects, primarily determines the type of defect species and their reducibility, while the overall extent of reduction is mainly governed by the amount of incorporated Ni.

The reduction process of the iron and nickel species was assessed in detail with XANES (Fig. 4). In the case of Fe (Fig. 4a), the structure does not appear to change with concentration and temperature of calcination. However, small changes can be observed in the metal-edge region (*i.e.* pre-peak P1 at 7114.4 eV), especially for the samples with 5% Fe, suggesting the formation of a metallic phase upon heating, provided the higher Fe content in the matrix. Conversely, in the case of Ni-STO (Fig. 4b), we observe a higher variability in the XANES region. For all the samples, we observe the formation of metallic Ni at 600 and 900 °C, with an increase in the signal at 8333.5 eV (P1 peak).

The concentration of the metallic fraction of Ni and Fe has been calculated using the LCF (whose results are shown in Table S2 and in Fig. S2, S3, and S4 in SI). The results indicate that for iron, the formation of the metal phase begins at a lower temperature, with a relative concentration of 4–11% of Fe at 400 °C; it remains stable until 600 °C and then increases until 900 °C, approximately doubling (21–28%). Nickel data, however, show that the formation of the metallic phases begins above 400 °C, and their concentration increases with temperature at a much higher rate than Fe. The rate of conversion of Ni in its metallic phase is proportional to the Fe and Ni concentrations in the structure: 1Ni-STO and 5Ni-STO show a final conversion of 23% and 45%, respectively, while the presence of Fe in the perovskite enhances the formation of metallic Ni up to in the range of 58–70%.

The analysis of EXAFS curves (Fig. S5 in SI) supports these conclusions, revealing that the profiles of Fe do not show changes apart from a new oscillation appearing at 9.4 Å, more pronounced in the samples heated at 900 °C, related to the formation of the metallic phase (Fig. S5, left). For the Ni edge, instead, it is possible to observe the high conversion from the perovskite structure to the metallic Ni structure (Fig. S5, right).

Fig. 5 better highlights the effects of the temperature treatment on the samples through the Fourier Transform of the EXAFS curves. Here, the formation of the metallic bond is marked by the appearance of the peak at 2.2 Å, related to the metallic first shell. As concerns the iron species (Fig. 5 left), the bond is barely visible in the 1Fe-STO sample, while it is mostly detectable in 5Fe-STO where the LCF also shows a higher iron reduction. Interestingly, this feature becomes more evident in co-doped perovskites and, specifically in 5Fe0.1Ni-STO after reduction at 900 °C, suggesting that even a tiny presence of Ni seems to enhance the iron exsolution. In the Ni curves (Fig. 5, right), besides an obvious peak related to the generation of Ni(0) in the materials with the highest metal doping (*i.e.*, 5Ni-STO), the presence of Fe in the perovskites promotes the formation of

Open Access Article. Published on 03 febbraio 2026. Downloaded on 31/05/2026 00:22:16.
This article is licensed under a Creative Commons Attribution-NonCommercial 3.0 Unported Licence.

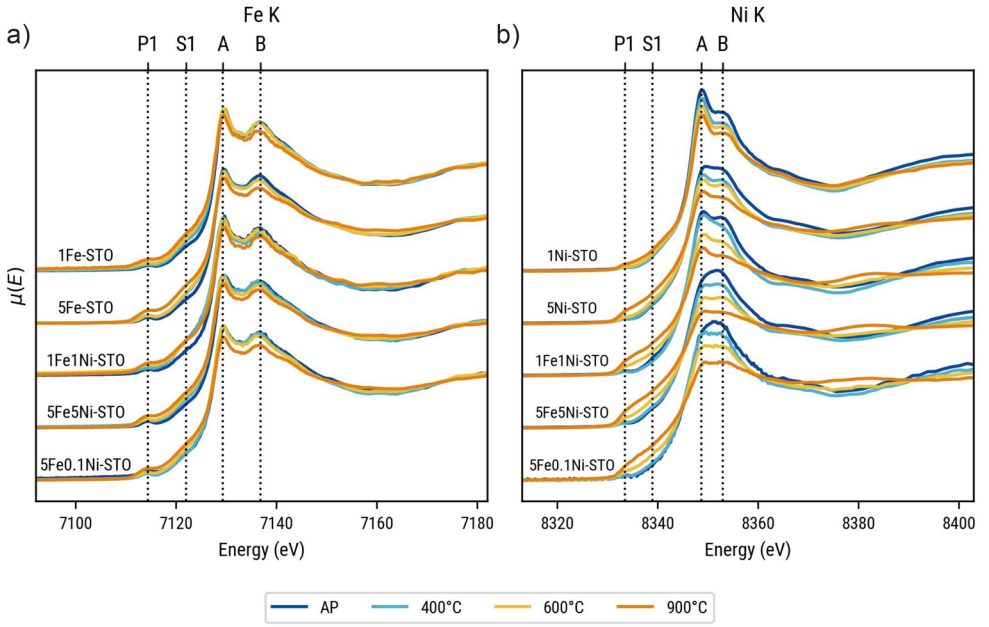

Fig. 4 XANES spectra of the undoped and doped perovskite samples recorded at the Fe K-edge (a) and Ni K-edge (b).

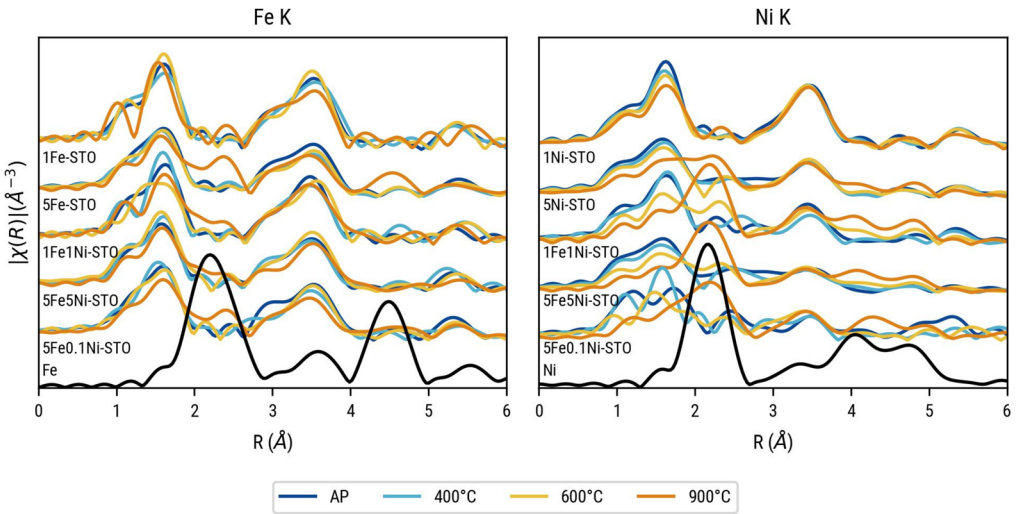

Fig. 5 Fourier Transform of the EXAFS region of the samples recorded at the Fe K-edge (column left) and Ni K-edge (column on the right). In black, the curve of the pure metal.

the metallic phase after heating, regardless of the Ni concentration. From the fit, we can observe that the distances of Ni inside the perovskite structure are stable regardless of the heat treatment, as can be observed from the results in Table S3 (see SI). The same can be observed from the data of Fe (Table S4): the perovskite structure remains stable regardless of the temperature, and at high temperature, the structure of metallic Fe is the same as the metallic BCC structure.

Beyond the previously mentioned analysis, STEM investigations enabled a detailed study of the morphological changes in Fe-STO, Ni-STO, and co-doped powders during the exsolution process. Fig. 6 presents STEM images and the corresponding EDX elemental mapping of Fe and Ni for the differently doped $SrTiO_3$ samples after exsolution at 900 °C. A comparative analysis of the images indicates that nearly all samples exhibit localized regions of increased dopant metal concentration, which are attributed to the presence of metal nanoparticles on the surface. Notably, the 5Fe-STO (Fig. 6a) displays a lower particle density and less well-defined particle boundaries relative to the other samples. This observation suggests that the exsolution process in this case may be incomplete, potentially reflecting a state of incipient segregation rather than fully developed nanoparticle formation. To further investigate the oxidation state of the surface Fe species, X-ray

 This journal is © the Partner Organisations 2026

Open Access Article. Published on 03 febbraio 2026. Downloaded on 31/05/2026 00:22:16.
This article is licensed under a Creative Commons Attribution-NonCommercial 3.0 Unported Licence.

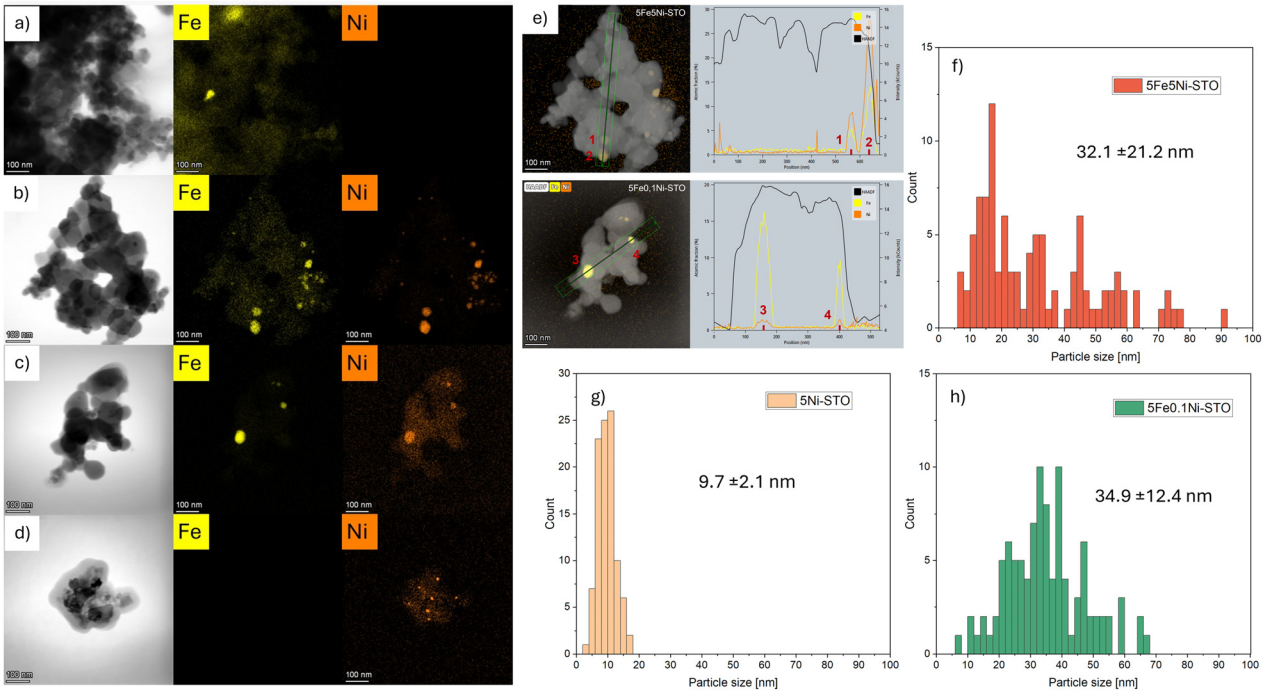

Fig. 6 STEM images and corresponding Fe and Ni EDX elemental maps after exsolution at 900 °C of (a) 5Fe-STO, (b) 5Fe5Ni-STO, (c) 5Fe0.1Ni-STO and (d) 5Ni-STO, respectively; (e) HAADF image and EDX mapping of Ni and Fe and the corresponding line scan; (f–h) particle size distribution of the corresponding *in situ* exsolved Ni–Fe and Ni nanoparticles shown in parts b–d calculated by using ImageJ software (counting on over 100 particles).

photoelectron spectroscopy (XPS) was employed, as detailed in the following section.

In agreement with XAS findings, the Fe-Ni co-doped samples (Fig. 6b and c) demonstrate a markedly enhanced exsolution behavior. TEM micrographs and corresponding EDX elemental maps reveal well-defined nanoparticles anchored to the perovskite surface. The overlap of Fe and Ni regions confirms their co-localization, indicating the formation of bimetallic or co-exsolved nanoparticles. According to PXRD and XAS, no alloy generation can be inferred with this low doping levels (see Fig. S7). The observed high particle density and uniform dispersion suggest a synergistic interaction between Fe and Ni that facilitates accelerated exsolution kinetics and improved nanoparticle stabilization. Remarkably, this effect is evident even at low Ni doping levels (*e.g.*, 5Fe0.1Ni-STO), where discrete surface nanoparticles are still clearly present, underscoring the pronounced sensitivity of the exsolution process to dopant composition.

Finally, consistent with previous reports in the literature,[9] Ni is capable of exsolving under reducing conditions even in the absence of Fe (Fig. 6d). The STEM image reveals isolated nanoparticles on the surface, and EDX analysis confirms that these regions contain only Ni, indicating the formation of pure Ni nanoparticles.

It should be pointed out that Fig. 6 provides an indication of the surface nature of the nanoparticles, as evidenced by their well-defined shapes in the compositional maps. In fact, blurring effects on the contours maps of Fe and Ni has to be expected whenever the particles are formed in the bulk grains of STO. Moreover, a clear deformation of the grains themselves would also be observed.

To further sustain this consideration a superimposed HAADF image combined with Fe and Ni elemental maps was acquired, along with the corresponding line scan (Fig. 6e). Well-resolved images of the particles are obtained without any evidence of grain deformation. Besides, the Fe and Ni signals clearly overlap, and no features other than those associated with the pure metallic species are detected.

The particle size distribution of the *in situ* exsolved Ni–Fe and Ni nanoparticles in 5Fe5Ni-STO, 5Fe0.1Ni-STO and 5Ni-STO are reported in Fig. 6f–h.

The surface chemical composition of the doped and co-doped $SrTiO_3$ perovskites was investigated by X-ray photoelectron spectroscopy (XPS) by measuring the Fe $2p_{3/2}$, Ni $2p_{3/2}$, Sr 3d, and Ti 2p core levels before and after reduction (XPS survey spectra and Sr 3d and Ti 2p regions are reported in Fig. S6).

Fig. 7 shows the Fe $2p_3/_2$ (a, c and e) and Ni $2p_3/_2$ (b, d and f) spectra of single-doped (5Fe-STO, 5Ni-STO) and co-doped (5Fe5Ni-STO, 5Fe0.1Ni-STO) samples, recorded before (bottom) and after reduction (top, labelled "R"). For the Fe 2p region, contributions from different Fe oxidized species are identified, while the Ni 2p region includes Ni^0, and other oxidized Ni components. Despite the difficulty in unambiguously assigning their oxidation states, these oxidized species exhibit energies comparable to pure compounds enclosing well-defined +2 and +3 Fe and Ni species.

Open Access Article. Published on 03 febbraio 2026. Downloaded on 31/05/2026 00:22:16.
This article is licensed under a Creative Commons Attribution-NonCommercial 3.0 Unported Licence.

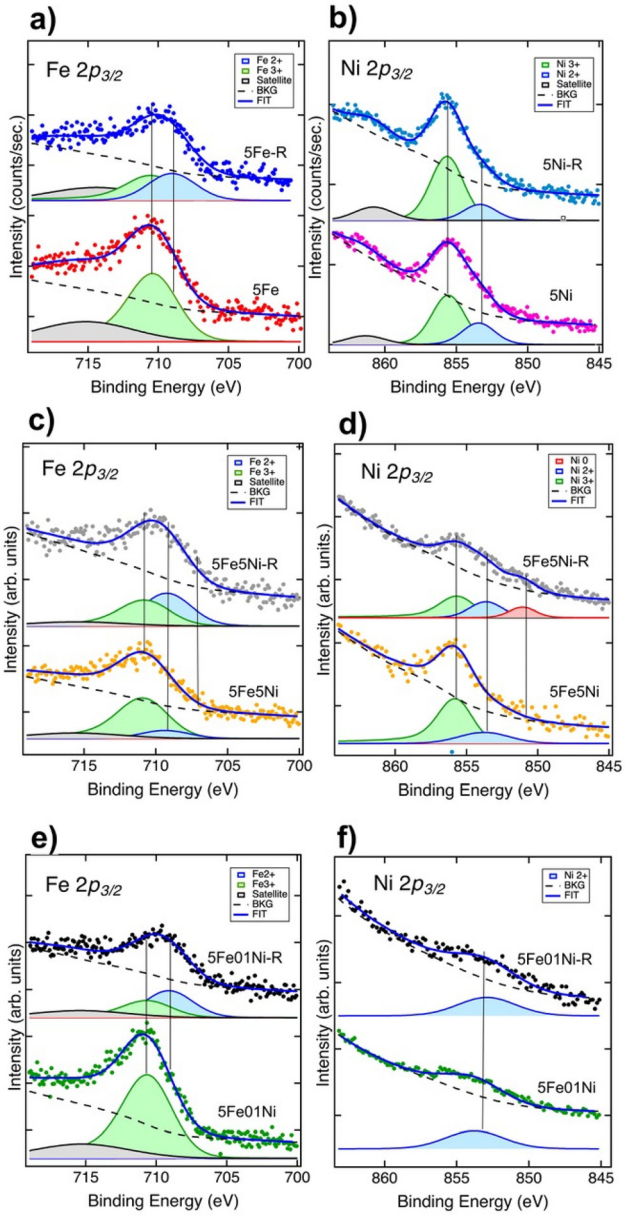

Fig. 7 Fe $2p_{3/2}$ (a, c and e) and Ni $2p_{3/2}$ (b, d and f) XPS spectra of single-doped (5Fe, 5Ni) and co-doped (5Fe5Ni, 5Fe0.1Ni) samples, recorded before (bottom) and after reduction (top, labelled with R).

Upon reduction, a faint yet discernible Ni(0) signal appears in the co-doped 5Fe5Ni-STO sample (Fig. 7d), whereas it is absent in the Ni-only system (Fig. 7b). This confirms the outcomes of XAS and STEM corroborating that Fe promotes the partial exsolution and reduction of Ni species. Because of the very low Ni signal in the 5Fe0.1Ni-STO sample, a similar reduction of Ni cannot be fully excluded, even if not clearly evident in the spectrum. Indeed, a slight shift of the Ni $2p_{3/2}$ peak towards lower binding energy is detected, although it may fall within the experimental uncertainty. These observations indicate that Fe facilitates Ni reduction, possibly through the creation of oxygen vacancies or modification of the local electronic structure. Conversely, Fe is consistently found in mixed oxidation states and becomes only slightly reduced after the reduction treatment, leading to predominant oxidized iron features (panels c and e), even when Ni is present.

These results, in addition to aligning with literature reports showing that iron exsolution generates oxidized iron species at the surface,[15] do not contradict the XAS findings but rather complement them. Indeed, XAS probes the entire bulk, whereas XPS is surface-sensitive. Consequently, Fe can appear oxidized at the surface while remaining in a reduced state within the bulk.

It should be observed that, during data acquisition, a certain degree of beam-induced reduction of the STO matrix cannot be excluded, even though a conventional laboratory X-ray source is used. This effect may have contributed to a partial reduction of the host lattice and, consequently, of the dopant species.

In any case, XPS analysis again substantiate the occurrence of a mutually synergistic interaction between Fe and Ni, which enhances both exsolution kinetics and particle stability.

To explore the evolution of defect structures in both mono-doped and co-doped STO samples during the exsolution process, an extensive X-band EPR study was also carried out. The spectra were recorded under vacuum conditions ($p < 10^{-5}$ mbar) at 130 K, following a reducing treatment in H_2/Ar at temperatures ranging from 400 to 900 °C. These measurements provide valuable insights into the coordination environment and aggregation state of metal ions, as well as the dynamic processes associated with the modification of the metal ions.

The EPR spectra collected for iron doped perovskites are summarized in Fig. 8. The spectrum of the as-prepared 1Fe-$SrTiO_3$ sample (Fig. 8a) reveals the presence of multiple Fe species. Specifically, several distinct peaks are observed in the low-field region (g = 9.8, g = 6.02, g = 4.84, see highlight of the low-field spectral region in the left panel of Fig. 8a), along with multiple spectral features in the mid-field region (g = 2.24, g = 2.00, g = 1.83). This complex signal pattern indicates that Fe ions are present in a variety of oxidation states and coordination environments within the $SrTiO_3$ lattice. Based on a survey of the literature, the observed g-values can be tentatively assigned to different Fe(II) and Fe(III) species (Table 1).[34–47]

The spectral complexity is further underscored by the changes observed during the treatment of the sample under a reducing atmosphere. Specifically, following thermal treatment at 400 °C, a moderate decrease in the intensity of the main signal at $g \approx 2$ is observed, while no further substantial changes are detected at higher temperatures (Fig. 8a). This behavior suggests that, during exsolution in 1Fe-STO, a minor fraction of iron species, likely located near the surface of the perovskite lattice and possibly associated with amorphous, interstitial Fe–O_x-like impurities, undergo selective reduction and migration, leading to the formation of zero-valent or diamagnetic Fe species. In contrast, the majority of Fe atoms, which are presumably incorporated as substitutional defects

 This journal is © the Partner Organisations 2026

Open Access Article. Published on 03 febbraio 2026. Downloaded on 31/05/2026 00:22:16.
This article is licensed under a Creative Commons Attribution-NonCommercial 3.0 Unported Licence.

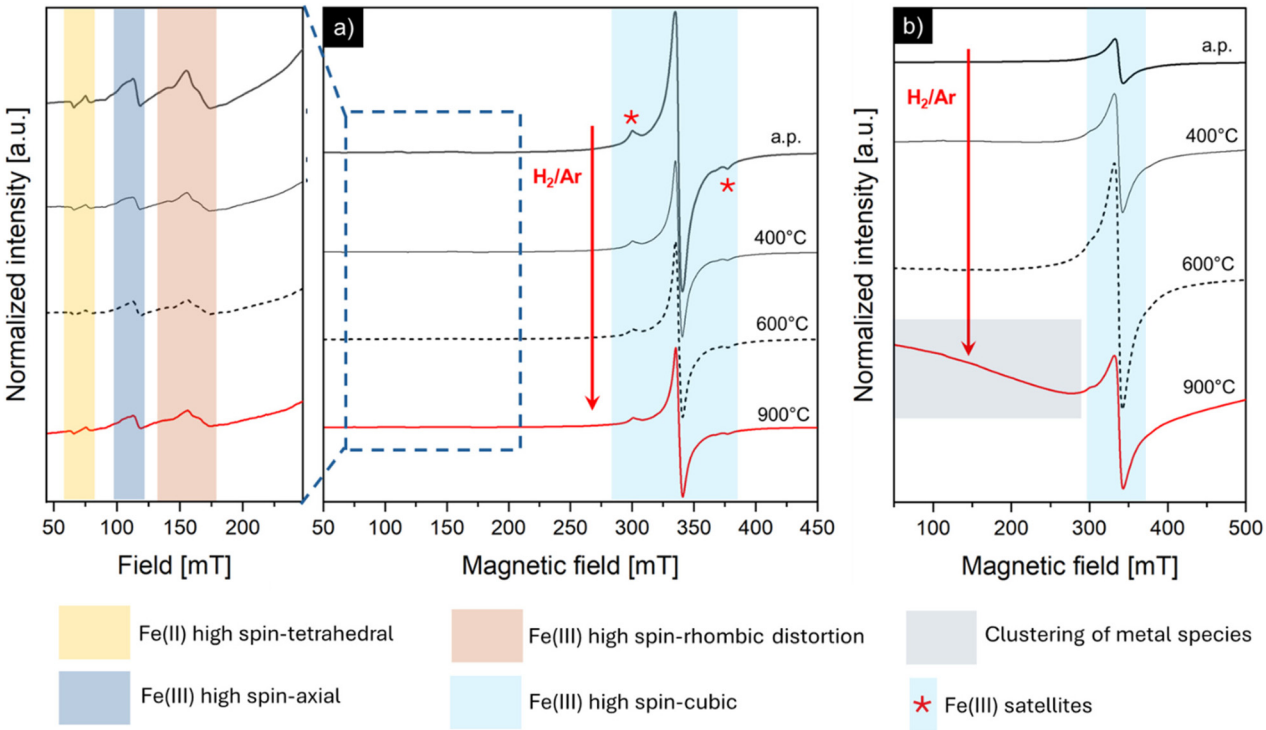

Fig. 8 EPR spectra at 130 K of (a) 1Fe-STO and (b) 5Fe-STO nanopowders as prepared (a.p.) and after thermal reduction at different temperatures in H_2/Ar atmosphere. The panel on the left highlights the iron-related signals detected at low magnetic field. A detailed description of the spectral features assignment is provided at the bottom (see also Table 1).

Table 1 *g*-Values and tentative attributions of the different Fe-centers detected in 1Fe-STO sample as obtained from literature survey

Metal species	Coordination	*g* value
Fe(II) high spin	Tetrahedral	$g_{\|\|} = 9.54$, $g_{\perp} = 4.33$
Fe(III) high spin – V_O	Axial	$g_{\|\|} = 6.02$, $g_{\perp} = 2.00$
Fe(III) high spin	Rhombic distortion	$g = 4.84$
Fe(III) high spin	Cubic	$g^{iso} \sim 2$ with two satellites ($A = 35$ mT)

within the perovskite lattice, remain unreduced even after treatment at 900 °C. This indicates the presence of highly stable defect sites, which require significantly higher thermal activation energy to become mobile and undergo reduction.

Upon increasing the iron dopant concentration (5Fe-STO sample), a similar behavior is observed (Fig. 8b). In this case, the EPR spectrum of the as-prepared material is dominated by broader features, which are attributed to dipolar interactions between closely spaced iron species. Unlike 1Fe-STO, a marked increase of the iron resonances is observed upon reduction of 5Fe-STO even at 400 °C. According to Drahus *et al.*[46,47] this trend may be connected to a change in iron oxidation-state, *i.e.* a part of the 'EPR-silent' Fe^{4+} or Fe^{+5} species, generally detectable in highly doped perovskites,[48] is converted into paramagnetic Fe^{3+}. Finally, when the reduction temperature is raised to 900 °C, the oxygen in the lattice of the perovskite gets reduced, fostering the reduction of dopant ions and thus leading to a remarkable depletion of the EPR signal. Moreover, the broadening of the spectral feature over the full spectral range highlights the occurrence of strongly dipolarly coupled Fe species, attributable to Fe-ion migration and subsequent aggregation into clustered or interacting structures.

Overall, these results evidenced that the chemical environment of iron species in Fe-STO is much more heterogeneous and the exsolution process is much less straightforward than expected.

A comparable analysis has also been applied to Ni-doped samples. Ni(II), as a d^8 ion, possesses two unpaired electrons, corresponding to a total spin state of $S = 1$. As such, it is susceptible to zero-field splitting (ZFS). When Ni(II) substitutes Ti (IV) within the perovskite lattice, charge compensation is typically achieved through the formation of oxygen vacancies (V_O). These vacancies can be located in the proximity of Ni centers, leading to the formation of defect complexes such as $(Ni\_Ti''\text{--}V_O^{\cdot\cdot})^X$ or $(Ni\_Ti' - V_O^{\cdot\cdot})^{\cdot}$.[43,49–51]

The spectra of 1Ni-STO show the presence of few different Ni species, probably due to the preferential intercalation rather than substitution of Ni ions in the perovskite lattice (Fig. 9a) associated with the larger ionic radius of Ni(II) species. When this intercalation happens Ni(II) can also be oxidised to Ni(III) and the centres present can be different. In particular, three different centres can be observed, two signal at $g \approx 2.20$ due to the presence of Ni(II) and Ni(III) in an octahedral

Open Access Article. Published on 03 febbraio 2026. Downloaded on 31/05/2026 00:22:16.
This article is licensed under a Creative Commons Attribution-NonCommercial 3.0 Unported Licence.

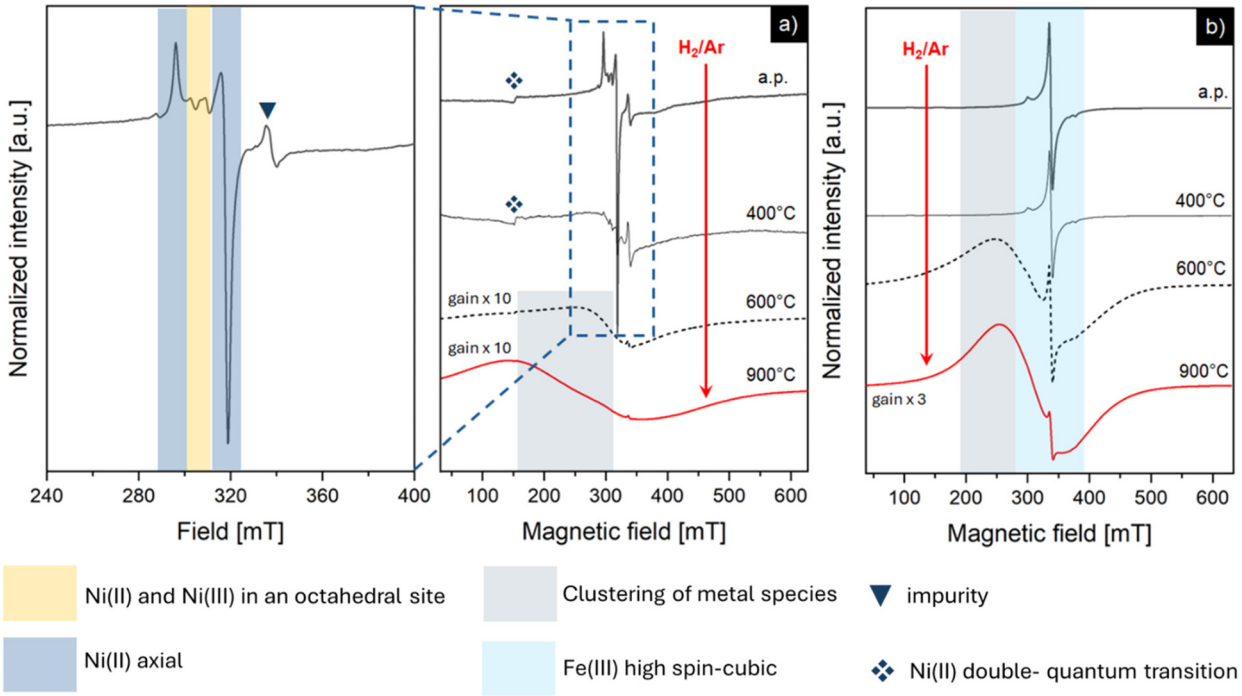

Fig. 9 EPR spectra at 130 K of (a) 1Ni-STO and (b) 1Fe1Ni-STO samples before and after thermal reduction at different temperatures in H_2/Ar.

site and a signal which may be tentatively attributed to an axial center with $g_{\parallel} = 2.31$ and $g_{\perp} = 2.12$.[51] Moreover, the signal at low-field related to double- quantum transitions of Ni(II) in oxides is clearly detectable.[52]

Upon reduction at 400 °C the signal intensity initially decreases due to the probable reduction of Ni(II) and Ni(III) to some EPR-silent species. This shows that intercalated Ni species, which has already been discovered in other studies[53–57] are the first being depleted, thus confirming recent computational studies attributing the origin of the exsolution process to interstitial metal sites.[55] In the present work EPR results indicate that a metal dopant such as nickel can be reduced within the perovskite lattice to Ni^{+} and even to Ni^{0}, but only if present as an interstitial and as part of an associate with an oxygen vacancy. This provides clear experimental evidence that strengthens such exsolution mechanism.

At 600 °C, the EPR signal intensity exhibits again an increase, accompanied by pronounced spectral broadening, which is consistent with the generation of multiple coupled Ni–Ni species due to aggregation or clustering of Ni centers. Nevertheless, even within the broadened spectrum, sharp signals corresponding to isolated Ni species remain discernible. This observation suggests the coexistence of Ni species with distinct redox behaviors, likely arising from differences in coordination environments or lattice incorporation. A very similar trend is observed for the 5Ni-STO sample (not shown). However, in this case magnetic coupling between paramagnetic centers is enhanced, resulting in dominant broad features in the spectrum which complicate the identification and resolution of individual Ni species.

Finally, the behavior of co-doped perovskite samples containing both Fe and Ni was investigated. Irrespective to Ni concentration, the EPR spectra of the as-prepared materials are dominated by features characteristic of Fe(III) species detected in iron doped perovskites. However, upon reduction, the samples exhibit markedly different behavior compared to the single metal doped materials.

In particular, the spectral evolution of 1Fe0.1Ni-STO sample is reported in Fig. 9b. Interestingly, besides the persistence of a signal at $g \approx 2$ related to isolated and non-reduced iron metal centers, the thermal treatment at 600 °C already results in the occurrence of a broad and intense feature associated with metal–metal coupling, consistent with the migration and spatial clustering of reduced metal ions. Upon further temperature increase, the overall signal broadening intensifies, reinforcing the interpretation of progressive metal aggregation and reduction. This indicates that the simultaneous incorporation of both metals within the perovskite lattice, even at very low concentrations (*e.g.*, 0.1% Ni), substantially enhances the exsolution process.

In summary, the EPR analysis highlights clear differences in the redox behavior of the two metal dopants. Specifically, Fe ions embedded within the perovskite lattice exhibit limited reducibility and a low tendency to exsolve, thus requiring higher thermal input for activation. In contrast, Ni ions are readily reduced and display higher mobility within the matrix. In co-doped perovskites, the overall behavior reflects a combination of the individual redox responses, even when the Ni content is minimal. These findings are consistent with XPS, where the presence of oxidized iron species at the surface are

 This journal is © the Partner Organisations 2026

Open Access Article. Published on 03 febbraio 2026. Downloaded on 31/05/2026 00:22:16.
This article is licensed under a Creative Commons Attribution-NonCommercial 3.0 Unported Licence.

detectable and with STEM observations, which highlight that perovskites doped solely with Fe show little to no particle formation after reduction, whereas FeNi-STO exhibit Fe–Ni co-exsolved nanoparticles decorating the oxide surface.

Catalytic performance

The prepared perovskites were evaluated for the CO_2 hydrogenation reaction, and specifically, for the production of CO through the reverse water gas shift reaction. The results obtained are presented in Fig. 10. CO and CH_4 were the only products detected during the experiments.

Since CO_2 hydrogenation to CO is an endothermic reaction, high-temperature operation is required to achieve significant CO_2 conversion and selectivity. In addition, lower pressure conditions are also beneficial to the reaction.[58]

As a general trend, the catalytic activity in terms of CO_2 conversion (Fig. 10a) increases with the increase in temperature with all catalysts reaching equilibrium values between 600 °C and 750 °C. As expected, the monometallic Fe-STO catalyst exhibited the lowest activity amongst all samples, which is attributed to the limited degree of Fe reduction at the surface (as confirmed by XPS results). Thus, the existence of FeO_x was responsible for the low CO_2 conversion and high CO selectivity achieved (considering that metallic Fe particles are the active phase in CO_2 methanation). Interestingly, the doping of Fe-STO even with low amounts of Ni (very low concentration of 0.1%), enhanced the overall catalytic activity (higher CO_2 values) across the entire temperature range.

The combination of NiFe in bimetallic systems supported on different oxides has been investigated in CO_2 hydrogenation and compared with the performance of monometallic Ni-based catalysts. As is well understood, the catalytic activity and product distribution (CH_4 or CO) strongly depends on the metal composition, oxidation state of the metals and to any alloy phases formed.[59] In particular, a number of research works report that, completely reduced Ni and Fe bimetallic systems outperform monometallic Ni-based catalysts in terms of X_{CO2}, with the main product obtained being CH_4. In contrast, the presence of metal oxides (especially FeO_x) direct instead the reaction towards the production of CO, with lower X_{CO2} values than the corresponding monometallic Ni catalysts.[60,61]

From the results presented herein, the best catalytic performance in terms of CO_2 conversion was achieved using the monometallic Ni catalyst (instead of the NiFe materials), a metal known for its deep hydrogenation properties, which directed the reaction mainly towards CH_4 between 400–550 °C. An additional observation is that both bimetallic NiFe catalysts, not only exhibited lower X_{CO2} values than the monometallic Ni, but also, were highly selective towards CO, despite the existence of Ni in the perovskite structure. These results are in agreement with the work of Piano *et al.*[62] who reported a decreased performance in the methanation activity on a Ni5Fe5 supported on SiO_2 or CeO_2-ZrO_2 catalyst compared to the monometallic Ni or the NiFe bimetallic systems with higher Ni loadings (*i.e.*, Ni9Fe1, Ni7.5Fe2.5). It is noted that the superior performance of the bimetallic catalysts reported in the literature for the methanation reaction has been attributed to the formation of the NiFe alloy phases (often Ni_3Fe) as well as metallic Fe (*via* the equation $Fe_3O_4 + Ni \rightarrow Fe + Ni_{1-x}Fe_x$), *i.e.*, these are the active sites that lead to higher CO_2 conversion and CH_4 selectivity on the NiFe

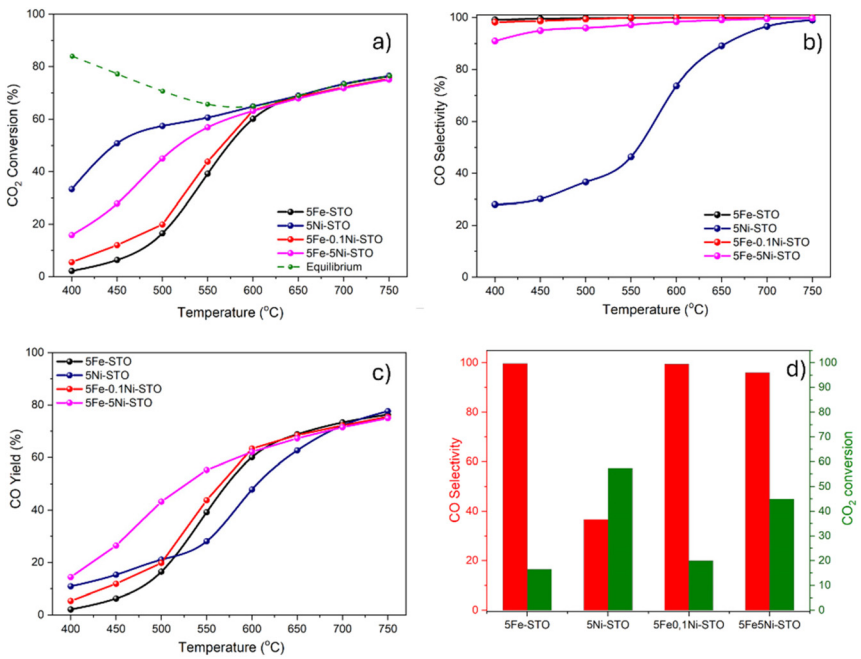

Fig. 10 Catalytic performance of Fe and Ni mono- and co-doped STO perovskites: (a) CO_2 conversion, (b) CO selectivity and (c) CO yield. Reaction conditions: T = 400 °C–750 °C, P = 1 atm, CO_2/H_2 = 1/4 and WHSV = 25 000 mL h^{-1} g^{-1}; (d) comparative trend of CO_2 conversion and selectivity for the tested samples at 500 °C.

Open Access Article. Published on 03 febbraio 2026. Downloaded on 31/05/2026 00:22:16.
This article is licensed under a Creative Commons Attribution-NonCommercial 3.0 Unported Licence.

bimetallic systems in comparison with the monometallic Ni catalyst.[63] Thus, although Fe exsolution and reduction was promoted by the addition of Ni on the catalysts tested herein, for all Fe-containing samples, CO was the main product, with selectivity values ranging from ~90% for the 5Fe-5Ni-STO to ~100% for the undoped 5Fe-STO even at the low reaction temperature of 400 °C. This result is attributed to the high number of unreduced Fe oxides (likely incorporated in the lattice as $SrFeTiO_3$) even after treatment at 900 °C. It is also noted that the PXRD and XAS showed the lack of any NiFe alloys. This result suggests the intrinsic nature of Fe oxides on catalyzing selectively the CO_2 reduction to CO (Fig. 10b).

Similar conclusions were drawn by Liu *et al.*[64] who, using a hybrid DBD plasma-catalysis system, reported that the integration of Ni in a $LaSrFeO_3$ catalyst (Ni/Fe = 1) led to higher dispersion and smaller size of metal particles, as well as to stronger metal–support interactions. The high CO selectivity reported was attributed to the incomplete reduction of Fe species (incorporated in the perovskite lattice as $LaSrFeO_3$) responsible for the existence of oxygen vacancies and the mobility of active oxygen, key parameters for the reverse water gas shift reaction *via* the redox mechanism.[21] This phenomenon is also illustrated in the results presented herein (Fig. 10c) in which the CO yield is markedly higher for the co-doped catalysts, with 5Fe-5Ni-STO outperforming both 5Fe-0.1Ni-STO and 5Fe-STO at the very low temperature range of 400 °C to 550 °C, suggesting the ability of the catalyst to balance both activity and selectivity, highlighting thus its potential as a high-efficiency RWGS catalyst. We note that studies in the literature related to the synergistic effect of Fe and Ni in perovskite structures for the thermo-catalytic conversion of CO_2 are scarce. The only one we found was carried out by Martin *et al.*[65] who studied a series of $Ln_{0.5}Ba_{0.5}Fe_{1-x}Ni_xO_3$ (Ln = Pr, Sm; and x = 0, 0.1) catalysts and observed a decrease in the reactivity of the Ni doped Fe catalysts compared to the monometallic Fe. However, as the authors noted, this result is rather surprising, considering both the very active nature of Ni and the higher amount of oxygen vacancies formed during reduction. The exegesis provided for this result was that the lattice oxygen of the Ni-doped exsolved materials was depleted.

Succinctly, regarding the catalytic results presented herein, the enhanced performance of the Fe–Ni co-doped samples can be attributed to the existence of a synergy between the metals, where Fe promotes the formation of oxygen vacancies and enhances redox activity and selectivity toward CO, while Ni facilitates H_2 dissociation and CO_2 conversion (Fig. 10d).

Conclusions

This work investigates the individual and cooperative effects of Ni and Fe on the bimetallic exsolution process from A-site-deficient $SrTiO_3$ perovskites. Specifically, a series of A-site-deficient oxides with the general formula $Sr_{0.95}Ti_{1-x+y}Fe_xNi_yO_{3\pm\delta}$ (x = 0, 0.01, 0.05; y = 0, 0.001, 0.01, 0.05) were successfully synthesized *via* a tailored sol–gel method. Surface decoration with metallic nanoparticles was achieved through redox-driven exsolution. By employing low doping levels and combining multiple characterization techniques the individual and cooperative roles of Ni and Fe in defect formation and metal nucleation at the surface was better delineated.

In particular, TPR results show that Fe doping primarily controls the formation and reducibility of oxygen-vacancy–associated defects, leading to the formation of reduced Fe species at relatively low temperatures. In contrast, Ni dictates the overall extent of reduction. XAS analysis further reveals that Ni-only samples undergo limited reduction to Ni(0), whereas co-doping with Fe significantly enhances Ni exsolution. Notably, even small amounts of Ni facilitate Fe reduction, as evidenced by EXAFS data.

Consistent with these findings, STEM imaging demonstrates the generation of well-anchored, surface-segregated Fe–Ni co-exsolved nanoparticles in co-doped perovskites, while Fe-only compositions show limited exsolution. Complementary XPS measurements indicate that surface Fe remains partially oxidized despite bulk reduction, reconciling the distinct probing depths of XAS and XPS techniques.

EPR spectroscopy provides additional validation of this mechanism by indicating that Fe species exhibit significantly lower reducibility and mobility compared to Ni. Fe is predominantly incorporated as highly stable Fe(III) substitutional defects within the perovskite lattice, and these species attain sufficient mobility to undergo surface segregation only upon concurrent incorporation of Ni. In contrast, Ni ions, owing to their larger ionic radius, preferentially occupy interstitial lattice positions, giving rise to oxidized Ni(III) species that constitute the first reducible sites under reducing conditions. This behavior aligns with recent DFT studies that attribute the initial stages of the exsolution process to the presence and reduction of interstitial metal cations.

These structure–property relationships translate directly to enhanced performance RWGS reaction for the co-doped materials, where Fe promotes the formation of oxygen vacancies and enhances redox activity and selectivity toward CO, while Ni facilitates H_2 dissociation and CO_2 conversion.

Overall, this study demonstrates that the analytical framework applied here can be extended to other exsolvable dopants (*e.g.*, Co), providing a basis for the rational design of exsolved catalysts with tunable compositions and architectures for advanced energy-conversion applications.

Conflicts of interest

There are no conflict to declare.

Data availability

The data supporting this article have been included as part of the supplementary information (SI). Supplementary information is available. See DOI: **https://doi.org/10.1039/d5qi02469b**.

This journal is © the Partner Organisations 2026

Open Access Article. Published on 03 febbraio 2026. Downloaded on 31/05/2026 00:22:16.
This article is licensed under a Creative Commons Attribution-NonCommercial 3.0 Unported Licence.

Acknowledgements

This research was funded by the European Union – NextGenerationEU, Italian National Recovery and Resilience Plan, Mission 4, Component 2, Investment 1.5 "Innovation Ecosystems", project "MUSA" and by within the framework of the Regional Programme of the European Regional Development Fund 2021–2027 of Regione Lombardia (PR FESR 2021-2027, Action 1.1.3, in compliance with European Regulation No. 1060/2021), following the public call "Collabora&Innova". Project "CO_2: from a global problem to a tool to implement circularity – CO-Tool" (Project ID 6144755). M. D. and P. M. gratefully thanks Dr Valeria Patini for the support in the experimental work. Angeliki I. Latsiou is grateful for financial support from the project "Funding of the Departments of Mechanical Engineering and Chemical Engineering of the University of Western Macedonia", Special Fee for Lignite Exploration and Exploitation Rights, Region of Western Macedonia, Greece.

References

1 K. Kousi, C. Tang, I. S. Metcalfe and D. Neagu, *Emergence and Future of Exsolved Materials*, John Wiley and Sons Inc., 2021. DOI: 10.1002/smll.202006479.

2 D. Neagu, *et al.*, Nano-socketed nickel particles with enhanced coking resistance grown in situ by redox exsolution, *Nat. Commun.*, 2015, **6**, 8120, DOI: 10.1038/ncomms9120.

3 D. Burnat, R. Kontic, L. Holzer, P. Steiger, D. Ferri and A. Heel, Smart material concept: Reversible microstructural self-regeneration for catalytic applications, *J. Mater. Chem. A*, 2016, **4**(30), 11939–11948, DOI: 10.1039/c6ta03417a.

4 S. Li, Q. Qin, K. Xie, Y. Wang and Y. Wu, High-performance fuel electrodes based on $NbTi_{0.5}M_{0.5}O_4$ (M = Ni, Cu) with reversible exsolution of the nano-catalyst for steam electrolysis, *J. Mater. Chem. A*, 2013, **1**(31), 8984–8993, DOI: 10.1039/c3ta10404d.

5 Y. R. Jo, *et al.*, Growth Kinetics of Individual Co Particles Ex-solved on $SrTi_{0.75}Co_{0.25}O_{3-\delta}$ Polycrystalline Perovskite Thin Films, *J. Am. Chem. Soc.*, 2019, **141**(16), 6690–6697, DOI: 10.1021/jacs.9b01882.

6 H. Lv, *et al.*, In Situ Investigation of Reversible Exsolution/Dissolution of CoFe Alloy Nanoparticles in a Co-Doped $Sr_2Fe_{1.5}Mo_{0.5}O_{6-\delta}$ Cathode for CO_2 Electrolysis, *Adv. Mater.*, 2020, **32**(6), 1906193, DOI: 10.1002/adma.201906193.

7 Y.-F. Sun, *et al.*, A-site-deficiency facilitated in situ growth of bimetallic Ni–Fe nano-alloys: a novel coking-tolerant fuel cell anode catalyst, *Nanoscale*, 2015, **7**(25), 11173–11181, DOI: 10.1039/C5NR02518D.

8 Y. Gao, J. Wang, Y. Q. Lyu, K. Lam and F. Ciucci, In situ growth of Pt_3Ni nanoparticles on an A-site deficient perovskite with enhanced activity for the oxygen reduction reaction, *J. Mater. Chem. A*, 2017, **5**(14), 6399–6404, DOI: 10.1039/c7ta00349h.

9 C. Tang, K. Kousi, D. Neagu and I. S. Metcalfe, Trends and Prospects of Bimetallic Exsolution, *Chem. – Eur. J.*, 2021, **27**(22), 6666–6675, DOI: 10.1002/chem.202004950.

10 O. Kwon, *et al.*, Self-assembled alloy nanoparticles in a layered double perovskite as a fuel oxidation catalyst for solid oxide fuel cells, *J. Mater. Chem. A*, 2018, **6**(33), 15947–15953, DOI: 10.1039/c8ta05105d.

11 Y. Jiang, *et al.*, Highly Efficient B-Site Exsolution Assisted by Co Doping in Lanthanum Ferrite toward High-Performance Electrocatalysts for Oxygen Evolution and Oxygen Reduction, *ACS Sustainable Chem. Eng.*, 2020, **8**(1), 302–310, DOI: 10.1021/acssuschemeng.9b05344.

12 Y. Wang, X. Lei, Y. Zhang, F. Chen and T. Liu, *In situ* growth of metallic nanoparticles on perovskite parent as a hydrogen electrode for solid oxide cells, *J. Power Sources*, 2018, **405**, 114–123, DOI: 10.1016/j.jpowsour.2018.10.023.

13 D. Papargyriou, D. N. Miller and J. T. S. Irvine, Exsolution of Fe–Ni alloy nanoparticles from $(La,Sr)(Cr,Fe,Ni)O_3$ perovskites as potential oxygen transport membrane catalysts for methane reforming, *J. Mater. Chem. A*, 2019, **7**(26), 15812–15822, DOI: 10.1039/C9TA03711J.

14 D. Neagu, G. Tsekouras, D. N. Miller, H. Ménard and J. T. S. Irvine, In situ growth of nanoparticles through control of non-stoichiometry, *Nat. Chem.*, 2013, **5**(11), 916–923, DOI: 10.1038/nchem.1773.

15 A. I. Tsiotsias, *et al.*, Bimetallic Exsolved Heterostructures of Controlled Composition with Tunable Catalytic Properties, *ACS Nano*, 2022, **16**(6), 8904–8916, DOI: 10.1021/acsnano.1c11111.

16 A. Anantha Krishnan, *et al.*, Multifunctional Na-enriched Ni–Fe/Ni–P plates for highly efficient photo- and electrocatalytic water splitting reactions, *New J. Chem.*, 2022, **46**(46), 22256–22267, DOI: 10.1039/D2NJ04389K.

17 W. Cheng, P. Fan and W. Jin, Visualizing the Structure and Dynamics of Transition Metal-Based Electrocatalysts Using Synchrotron X-Ray Absorption Spectroscopy, *ChemSusChem*, 2025, **18**(4), e202401306, DOI: 10.1002/cssc.202401306.

18 L. Kapokova, *et al.*, Dry reforming of methane over $LnFe_{0.7}Ni_{0.3}O_{3-\delta}$ perovskites: Influence of Ln nature, *Catal. Today*, 2011, **164**(1), 227–233, DOI: 10.1016/j.cattod.2010.10.086.

19 E. I. Papaioannou, D. Neagu, W. K. W. Ramli, J. T. S. Irvine and I. S. Metcalfe, Sulfur-Tolerant, Exsolved Fe–Ni Alloy Nanoparticles for CO Oxidation, *Top. Catal.*, 2019, **62**(17), 1149–1156, DOI: 10.1007/s11244-018-1053-8.

20 F. Orsini, *et al.*, Exsolution-enhanced reverse water-gas shift chemical looping activity of $Sr_2FeMo_{0.6}Ni_{0.4}O_{6-\delta}$ double perovskite, *Chem. Eng. J.*, 2023, **475**, 146083, DOI: 10.1016/j.cej.2023.146083.

21 L. Lindenthal, *et al.*, Novel perovskite catalysts for CO_2 utilization – Exsolution enhanced reverse water-gas shift activity, *Appl. Catal., B*, 2021, **292**, 120183, DOI: 10.1016/j.apcatb.2021.120183.

22 P. Mariani, *et al.*, Critical assessment of the exsolution process in Cu-doped $SrTiO_3$ by a combined spectroscopic

Open Access Article. Published on 03 febbraio 2026. Downloaded on 31/05/2026 00:22:16.
This article is licensed under a Creative Commons Attribution-NonCommercial 3.0 Unported Licence.

approach, Inorg, *Chem. Front.*, 2025, **12**(1), 311–327, DOI: 10.1039/D4QI02391A.

23 E. Calì, *et al.*, Exsolution of Catalytically Active Iridium Nanoparticles from Strontium Titanate, *ACS Appl. Mater. Interfaces*, 2020, **12**(33), 37444–37453, DOI: 10.1021/acsami.0c08928.

24 W. O'Leary, L. Giordano, J. Park, S. S. Nonnenmann, Y. Shao-Horn and J. L. M. Rupp, Influence of Sr-Site Deficiency, Ca/Ba/La Doping on the Exsolution of Ni from $SrTiO_3$, *J. Am. Chem. Soc.*, 2023, **145**(25), 13768–13779, DOI: 10.1021/jacs.2c12011.

25 F. d'Acapito, *et al.*, The LISA beamline at ESRF, *J. Synchrotron Radiat.*, 2019, **26**(2), 551–558, DOI: 10.1107/S160057751801843X.

26 G. Bellotti, *et al.*, ARDESIA Detection Module: A Four-Channel Array of SDDs for Mcps X-Ray Spectroscopy in Synchrotron Radiation Applications, *IEEE Trans. Nucl. Sci.*, 2018, **65**(7), 1355–1364, DOI: 10.1109/TNS.2018.2838673.

27 B. Ravel and M. Newville, ATHENA, ARTEMIS, HEPHAESTUS: Data analysis for X-ray absorption spectroscopy using IFEFFIT, *J. Synchrotron Radiat.*, 2005, 537–541, DOI: 10.1107/S0909049505012719.

28 M. Newville, Larch: An Analysis Package for XAFS and Related Spectroscopies, *J. Phys.: Conf. Ser.*, 2013, **430**(1), 012007, DOI: 10.1088/1742-6596/430/1/012007.

29 A. L. Ankudinov, B. Ravel, J. J. Rehr and S. D. Conradson, Real-space multiple-scattering calculation and interpretation of X-ray-absorption near-edge structure, *Phys. Rev. B: Condens. Matter Mater. Phys.*, 1998, **58**(12), 7565–7576, DOI: 10.1103/PhysRevB.58.7565.

30 R. J. Nelmes, G. M. Meyer and J. Hutton, Thermal motion in $SrTiO_3$ at room temperature: Anharmonic or disordered?, *Ferroelectrics*, 1978, **21**(1), 461–462, DOI: 10.1080/00150197808237297.

31 B. Koo, K. Kim, J. K. Kim, H. Kwon, J. W. Han and W. Jung, Sr Segregation in Perovskite Oxides: Why It Happens and How It Exists, *Joule*, 2018, **2**(8), 1476–1499, DOI: 10.1016/j.joule.2018.07.016.

32 L. F. da Silva, *et al.*, Relationship between Crystal Shape, Photoluminescence, and Local Structure in $SrTiO_3$ Synthesized by Microwave-Assisted Hydrothermal Method, *J. Nanomater.*, 2012, **2012**(1), 890397, DOI: 10.1155/2012/890397.

33 M. Vračar, *et al.*, Jahn-Teller distortion around Fe(IV) in Sr($Fe_xTi_{1-x}O_{3-\delta}$) from X-ray absorption spectroscopy, X-ray diffraction, and vibrational spectroscopy, *Phys. Rev. B: Condens. Matter Mater. Phys.*, 2007, **76**(17), 174107, DOI: 10.1103/PhysRevB.76.174107.

34 N. Pathak, S. K. Gupta, K. Sanyal, M. Kumar, R. M. Kadam and V. Natarajan, Photoluminescence and EPR studies on Fe^{3+} doped $ZnAl_2O_4$: an evidence for local site swapping of Fe^{3+} and formation of inverse and normal phase, *Dalton Trans.*, 2014, **43**(24), 9313–9323, DOI: 10.1039/C4DT00741G.

35 Y. J. Park, *et al.*, A mixed-valent Fe(II)Fe(III) species converts cysteine to an oxazolone/thioamide pair in methanobactin biosynthesis, *Proc. Natl. Acad. Sci. U. S. A.*, 2022, **119**(13), e2123566119, DOI: 10.1073/pnas.2123566119.

36 R. Merkle and J. Maier, Defect association in acceptor-doped $SrTiO_3$: case study for $Fe'Ti V_O^{\bullet\bullet}$ and $Mn''Ti V_O^{\bullet\bullet}$, *Phys. Chem. Chem. Phys.*, 2003, **5**(11), 2297–2303, DOI: 10.1039/B300205P.

37 E. S. Kirkpatrick, K. A. Müller and R. S. Rubins, Strong Axial Electron Paramagnetic Resonance Spectrum of Fe^{3+} in $SrTiO_3$ Due to Nearest-Neighbor Charge Compensation, *Phys. Rev.*, 1964, **135**(1A), A86–A90, DOI: 10.1103/PhysRev.135.A86.

38 C. Lenser, *et al.*, Spectroscopic study of the electric field induced valence change of Fe-defect centers in $SrTiO_3$, *Phys. Chem. Chem. Phys.*, 2011, **13**(46), 20779–20786, DOI: 10.1039/C1CP21973A.

39 J. Dashdorj, M. E. Zvanut and L. J. Stanley, Iron-related defect levels in $SrTiO_3$ measured by photoelectron paramagnetic resonance spectroscopy, *J. Appl. Phys.*, 2010, **107**(8), 083513, DOI: 10.1063/1.3372760.

40 H. H. Wickman, M. P. Klein and D. A. Shirley, Paramagnetic Resonance of Fe^{3+} in Polycrystalline Ferrichrome A, *J. Chem. Phys.*, 1965, **42**(6), 2113–2117, DOI: 10.1063/1.1696253.

41 R. W. Kedzie, D. H. Lyons and M. Kestigian, Paramagnetic Resonance of the Fe^{3+} Ion in $CaWO_4$ (Strong Tetragonal Crystal Field), *Phys. Rev.*, 1965, **138**(3A), A918–A924, DOI: 10.1103/PhysRev.138.A918.

42 S. Anderson, Paramagnetic Resonance of Iron in Glass, *J. Chem. Phys.*, 1969, **50**(6), 2783–2784, DOI: 10.1063/1.1671460.

43 B. Faughnan and Z. Kiss, Optical and EPR studies of photochromic $SrTiO_3$ doped with Fe/Mo and Ni/Mo, *IEEE J. Quantum Electron.*, 1969, **5**(1), 17–21, DOI: 10.1109/JQE.1969.1075665.

44 M. Nayak and T. R. N. Kutty, Luminescence of Fe^{3+} doped $NaAlSiO_4$ prepared by gel to crystallite conversion, *Mater. Chem. Phys.*, 1998, **57**(2), 138–146, DOI: 10.1016/S0254-0584(98)00209-0.

45 R. Merkle and J. Maier, Defect association in acceptor-doped $SrTiO_3$: case study for $Fe'Ti V_O^{\bullet\bullet}$ and $Mn''Ti V_O^{\bullet\bullet}$, *Phys. Chem. Chem. Phys.*, 2003, **5**(11), 2297–2303, DOI: 10.1039/B300205P.

46 M. D. Drahus, P. Jakes, E. Erdem and R.-A. Eichel, Defect structure of the mixed ionic–electronic conducting Sr[Ti,Fe]Ox solid-solution system—Change in iron oxidation states and defect complexation, *Solid State Ionics*, 2011, **184**(1), 47–51, DOI: 10.1016/j.ssi.2010.09.045.

47 M. Knight, I. Reimanis, A. Meyer, J.-H. Preusker and W. Rheinheimer, Dilute iron-doped polycrystalline strontium titanate: Tracking iron valence and local interactions, *J. Am. Ceram. Soc.*, 2023, **106**(8), 4740–4751, DOI: 10.1111/jace.19111.

48 E. Poffe, *et al.*, Understanding Oxygen Release from Nanoporous Perovskite Oxides and Its Effect on the Catalytic Oxidation of CH_4 and CO, *ACS Appl. Mater. Interfaces*, 2021, **13**(21), 25483–25492, DOI: 10.1021/acsami.1c02281.

 This journal is © the Partner Organisations 2026

Open Access Article. Published on 03 febbraio 2026. Downloaded on 31/05/2026 00:22:16.
This article is licensed under a Creative Commons Attribution-NonCommercial 3.0 Unported Licence.

49 M. Chiesa and E. Giamello, On the Role and Applications of Electron Magnetic Resonance Techniques in Surface Chemistry and Heterogeneous Catalysis, *Catal. Lett.*, 2021, **151**(12), 3417–3436, DOI: **10.1007/s10562-021-03576-x**.

50 K. A. Müller, W. Berlinger and R. S. Rubins, Observation of Two Charged States of a Nickel-Oxygen Vacancy Pair in $SrTiO_3$ by Paramagnetic Resonance, *Phys. Rev.*, 1969, **186**(2), 361–371, DOI: **10.1103/PhysRev.186.361**.

51 K. A. Müller, W. Berlinger and R. S. Rubins, Observation of Two Charged States of a Nickel-Oxygen Vacancy Pair in $SrTiO_3$ by Paramagnetic Resonance, *Phys. Rev.*, 1969, **186**(2), 361–371, DOI: **10.1103/PhysRev.186.361**.

52 K. Thangavel, *et al.*, Unveiling the atomistic and electronic structure of NiII–NO adduct in a MOF-based catalyst by EPR spectroscopy and quantum chemical modelling, *Phys. Chem. Chem. Phys.*, 2023, **25**(23), 15702–15714, DOI: **10.1039/D3CP01449E**.

53 S. Yang, S. Zhang, C. Sun, X. Ye and Z. Wen, Lattice Incorporation of Cu^{2+} into the $BaCe_{0.7}Zr_{0.1}Y_{0.1}Yb_{0.1}O_{3-\delta}$ Electrolyte on Boosting Its Sintering and Proton-Conducting Abilities for Reversible Solid Oxide Cells, *ACS Appl. Mater. Interfaces*, 2018, **10**(49), 42387–42396, DOI: **10.1021/acsami.8b15402**.

54 J. M. Polfus, M.-L. Fontaine, A. Thøgersen, M. Riktor, T. Norby and R. Bredesen, Solubility of transition metal interstitials in proton conducting $BaZrO_3$ and similar perovskite oxides, *J. Mater. Chem. A*, 2016, **4**(21), 8105–8112, DOI: **10.1039/C6TA02377K**.

55 A. Bonkowski, M. J. Wolf, J. Wu, S. C. Parker, A. Klein and R. A. De Souza, A Single Model for the Thermodynamics and Kinetics of Metal Exsolution from Perovskite Oxides, *J. Am. Chem. Soc.*, 2024, **146**(33), 23012–23021, DOI: **10.1021/jacs.4c03412**.

56 W. Wei, J. Gebhardt, D. F. Urban and C. Elsässer, Location and migration of interstitial Li ions in $CsPbI_3$ crystals, *Phys. Rev. B*, 2024, **109**(14), 144104, DOI: **10.1103/PhysRevB.109.144104**.

57 J. Luong, *et al.*, Nanoscale Iron Redistribution during Thermochemical Decomposition of $CaTi_{1-x}Fe_xO_{3-\delta}$ Alters the Electrical Transport Pathway: Implications for Oxygen-Transport Membranes, Electrocatalysis, and Photocatalysis, *ACS Appl. Nano Mater.*, 2023, **6**(3), 1620–1630, DOI: **10.1021/acsanm.2c04537**.

58 C. Zhou, J. Zhang, Y. Fu, and H. Dai, *Recent Advances in the Reverse Water–Gas Conversion Reaction*, Multidisciplinary Digital Publishing Institute (MDPI), 2023. DOI: **10.3390/molecules28227657**.

59 P. Yan, *et al.*, Unlocking the role of Ni-Fe species in CO_2 methanation, *Fuel*, 2024, **374**, 132373, DOI: **10.1016/j.fuel.2024.132373**.

60 A. Z. Md Azmi, *et al.*, The impact bimetallic Ni–Fe deposit configuration has on accessing synergy during plasma-catalytic CO_2 methanation, *Catal. Sci. Technol.*, 2025, **15**(11), 3372–3384, DOI: **10.1039/d5cy00036j**.

61 B. Mutz, *et al.*, Potential of an Alumina-Supported Ni_3Fe Catalyst in the Methanation of CO_2: Impact of Alloy Formation on Activity and Stability, *ACS Catal.*, 2017, **7**(10), 6802–6814, DOI: **10.1021/acscatal.7b01896**.

62 G. De Piano, J. J. A. Gamboa, A. M. Condó, S. Bengió and F. C. Gennari, Bimetallic Ni-Fe catalysts for methanation of CO_2: Effect of the support nature and reducibility, *Appl. Catal., A*, 2022, **634**, 118540, DOI: **10.1016/j.apcata.2022.118540**.

63 P. Wu, J. Sun, M. Abbas, P. Wang, Y. Chen and J. Chen, Hydrophobic SiO_2 supported Fe-Ni bimetallic catalyst for the production of high-calorie synthetic natural gas, *Appl. Catal., A*, 2020, **590**, 117302, DOI: **10.1016/j.apcata.2019.117302**.

64 L. Liu, *et al.*, Low temperature catalytic reverse water-gas shift reaction over perovskite catalysts in DBD plasma, *Appl. Catal., B*, 2020, **265**, 118573, DOI: **10.1016/j.apcatb.2019.118573**.

65 A. M. Martin, S. Saini, D. Neagu, W. Hu, I. S. Metcalfe and K. Kousi, Tailoring the A and B site of Fe-based perovskites for high selectivity in the reverse water-gas shift reaction, *J. CO2 Util.*, 2024, **83**, 102784, DOI: **10.1016/j.jcou.2024.102784**.